



Improving the optical, electrical and dielectric characteristics of ZnO nanoparticles through (Fe + Al) addition for optoelectronic applications

H. Saadi¹ · Z. Benzarti¹ · P. Sanguino² · Y. Hadouch³ · D. Mezzane³ · K. Khirouni⁴ · N. Abdelmoula¹ · H. Khemakhem¹

Received: 19 May 2022 / Accepted: 4 July 2022 / Published online: 18 July 2022
© The Author(s), under exclusive licence to Springer-Verlag GmbH, DE part of Springer Nature 2022

Abstract

In the present study, undoped ZnO and co-doped $\text{Zn}_{(0.99-x)}\text{Fe}_{0.01}\text{Al}_x\text{O}$ ($x=0.01, 0.03$ and 0.05) were effectively prepared by the co-precipitation process. The structural, morphological, optical and electrical properties were investigated in order to explore the effect of concentration of co-doped Al on the physical properties of ZnO nanopowders. Besides, the structural analysis revealed the formation of the hexagonal wurtzite structure of all the powdered compositions. The crystallite size was found to decline with Fe and Al incorporation into ZnO crystal lattice. An additional peak attributed to the secondary phase Al was also noted for the $\text{Zn}_{0.94}\text{Fe}_{0.01}\text{Al}_{0.05}\text{O}$ sample. Moreover, the morphological study suggested the change in the morphology of ZnO nanoparticles at higher Al co-doping concentrations and proved the formation of the secondary phase Al for the $\text{Zn}_{0.94}\text{Fe}_{0.01}\text{Al}_{0.05}\text{O}$ composition. Concerning optical properties, the optical band gap energy was found to decline with increasing Al co-doping concentration. An increasing trend of the Urbach energy was noted due to Fe/Al co-doping. Furthermore, the electrical and dielectric characterizations were performed in the same range of frequency and temperature. The obtained results showed that the dielectric constant was gradually increased with the rise of Al concentration. The electrical conductivity of ZnO nanopowder samples was also enhanced under the incorporation of Al into the ZnO matrix. This contribution enhances the understanding of optical and electrical properties of Fe/Al co-doped ZnO nanopowders for optoelectronic applications.

Keywords Fe/Al co-doped ZnO · Co-precipitation method · Structural analysis · Optical properties · Morphological properties · Electrical study

1 Introduction

Over the past few decades, several researchers have strongly focused their interest on the synthesis and the characterization of transition metal oxide semiconductors thanks to their superior properties [1]. Such semiconductor materials were evaluated extensively and were well documented due to their distinguished performance and potential applications in different fields [2–11]. Particularly, zinc oxide nanostructures (ZnO) have recently attracted the immense attention from the scientific community worldwide because of their numerous advantages as compared to the others oxide materials. This transition metal oxide is characterized by the non-toxicity, abundant resources, inexpensive production, good thermal and chemical stability, high transparency in the visible range and valuable piezoelectric properties [1, 3]. Zinc oxide nanomaterial is a II–VI semiconductor with a broad direct band gap of about 3.37 eV and a large exciton binding energy of

✉ H. Saadi
hajermosbahsaadi@gmail.com

¹ Laboratory of Multifunctional Materials and Applications (LaMMA), Department of Physics, Faculty of Sciences of Sfax, University of Sfax, Soukra Road km 3.5, B.P. 1171, 3000 Sfax, Tunisia

² CEMMPRE, Department of Mechanical Engineering, University of Coimbra, Rua Luis Reis Santos, Pinhal de Marrocos, 3030-788 Coimbra, Portugal

³ LMCN, Cadi Ayyad University, 40000 Marrakesh, Morocco

⁴ Laboratory of Physics of Materials and Nanomaterials Applied at Environment (LaPhyMNE), Faculty of Sciences of Gabes, University of Gabes, 6072 Gabes, Tunisia

60 meV at room temperature. Generally, zinc oxide is crystallized in hexagonal wurtzite structure which is considered as the most stable structure under the normal conditions [2, 12]. Moreover, the outstanding properties of ZnO, like its broad direct band gap and electric polarization behavior, make it a potential candidate for dielectric materials. All these excellent characteristics allow a prevalent material to be used in various applications, namely, spintronic [13], solar energy [14] photocatalytic [15] and antibacterial activity [16]. Synthesis methods have drastic impact on the material, and different methods have been adopted for the synthesis of ZnO nanomaterials, such as co-precipitation [13], hydrothermal [14], sol-gel [16] and solid-state reaction [17]. Nevertheless, in comparison with other synthesized routes, the co-precipitation process is widely used owing to its simplicity, low temperature, superior uniformity and homogeneity of the products, stability, less surface imperfection, rapid preparation and ease to control the shape and the size of the nanoparticles [5, 18]. Various successful approaches have been employed for modifying the structural, morphological, optical and electrical properties of ZnO nanostructures by co-doping with specific elements. Several researches have focused their interest on the change of physical characteristics of ZnO by transition metal incorporation [19–21]. In this context, doping ZnO with transition metals can significantly modify the morphology, particle size and the band gap energy by creating structural imperfections and defects in the lattice [19]. In addition, strong modification of electrical and dielectric characteristics of ZnO was reported by doping with transition metal elements thanks to their specific shell structure [4]. Particularly, the effect of Fe incorporation into ZnO crystal lattice was widely studied [22, 23]. Specifically, the improvement of optical and electrical properties of ZnO nanopowders prepared by co-precipitation method was achieved in our previous works [4, 24]. Further, the effect of Fe concentration on the structural, vibrational and dielectric behaviors of ZnO nanomaterials was reported by Bouslama et al. [19]. Their examination revealed the semiconductor nature of the investigated samples and suggested that the dominant conduction mechanism is assured by the process of small polaron hopping (SPH). In their investigation, the non-Debye type of relaxation process and the existence of the short range mobility of charge carriers in the prepared compositions was also affirmed by the modulus analysis. Actually, the enhancement of electrical behavior of ZnO and iron doped ZnO nanostructures by co-doping effect is not well documented. Besides iron doping, group III elements (B, Al, Ga, In, etc.) provide a successful tool for developing optical and electrical characteristics of ZnO nanomaterials, which are extensively developed for photoelectrodes in photovoltaic and optoelectronic devices [12]. Especially, Al incorporation into ZnO host matrix is interesting thanks to its elevated electrical conductivity, small ionic radius and

environmentally friendly matter. Several research teams studied the impact of simultaneous doping of Fe and Al on the structural, optical, morphological, photocatalytic and magnetic studies of ZnO nanostructures [25–27]. However, the electric and dielectric characteristics of Fe/Al co-doped ZnO nanopowdered compositions are less investigated compared to its other properties. The present investigation lies to check the effect of changing Al concentration on the various characteristics of ZnO nanomaterial prepared by the chemical co-precipitation approach. The enhancement of the optical and electrical characteristics of ZnO under Fe/Al co-doping makes the obtained co-doped ZnO samples to be promising candidates for the use in optoelectronics. In this study, Fe/Al co-doped ZnO nanoparticles at fixed Fe doping concentration 1% and different Al co-doping concentrations from 0 to 5% were synthesized by the co-precipitation method using $\text{ZnCl}_2 \cdot 4\text{H}_2\text{O}$, $\text{FeCl}_3 \cdot 6\text{H}_2\text{O}$ and $\text{AlCl}_3 \cdot 6\text{H}_2\text{O}$ as precursors. The purpose is to explore the impact of Al addition and its co-doping concentration on the structural, vibrational, optical, morphological, dielectric and electrical characteristics of ZnO nanostructures.

2 Experiments

2.1 Nanopowder synthesis

Undoped ZnO and co-doped $\text{Zn}_{(0.99-x)}\text{Fe}_{0.01}\text{Al}_x\text{O}$ ($x = 0.01, 0.03$ and 0.05) nanoparticles were synthesized by the co-precipitation approach. In this experiment, zinc chloride $\text{ZnCl}_2 \cdot 4\text{H}_2\text{O}$ (Sigma-Aldrich $\geq 99.995\%$ purity), ferric chloride hexahydrate $\text{FeCl}_3 \cdot 6\text{H}_2\text{O}$ (Sigma-Aldrich $\geq 98\%$ purity) and aluminum chloride tetrahydrate $\text{AlCl}_3 \cdot 6\text{H}_2\text{O}$ (Sigma-Aldrich $\geq 98\%$ purity) were used as starting precursor and doping precursors for iron and aluminum elements, respectively. For synthesis of undoped ZnO, 3.35 g of $\text{ZnCl}_2 \cdot 4\text{H}_2\text{O}$ was dissolved in 100 ml of deionized water. This starting solution was continuously stirred for 15 min at room temperature to get homogenous and stable mixture. Concerning the aqueous NaOH solution, it was separately prepared by dissolving 4 g of NaOH in 50 ml of deionized water through 15 min under constant magnetic stirring. Then, it was added drop by drop into the starting ($\text{ZnCl}_2 \cdot 4\text{H}_2\text{O}$) solution. After a complete mixture of ($\text{ZnCl}_2 \cdot 4\text{H}_2\text{O}$) and NaOH solutions, magnetic stirring was continued for 3 h to obtain white gel. Subsequently, the obtained white precipitate was washed many times with deionized water and absolute ethanol (Sigma-Aldrich $\geq 99.9\%$ purity). This step is necessary and it is repeated several times for the removal of any unreacted precursors. Afterwards, the formed gel was dried at 80°C for 12 h and then calcined at 500°C for 5 h. The same procedure was also adopted to synthesize $\text{Zn}_{(0.99-x)}\text{Fe}_{0.01}\text{Al}_x\text{O}$ ($x = 0.01, 0.03$ and 0.05) nanopowdered samples.

2.2 Characterization techniques

The prepared compositions were characterized by various characterization techniques in order to explore the impact of simultaneous doping of Fe and Al on the different characteristics of undoped ZnO nanostructures. Phase composition of the samples was verified by the utilization of a Bruker D8 Advanced X-ray diffractometer with $\text{CuK}\alpha$ radiation ($\alpha = 1.54056 \text{ \AA}$). Fourier transformed infrared (FTIR) spectroscopy (Perkin Elmer-spectrometer) in the wavenumber range of $400\text{--}4000 \text{ cm}^{-1}$ was used to investigate the vibrational properties. Concerning the optical characteristics, they were measured with a UV-vis spectrometer (SHIMADZU UV 3100S) in the wavelength range of $200\text{--}800 \text{ nm}$. The morphological properties of the nanoparticles were characterized by (high resolution) transmission electron microscopy (HRTEM) (Tecnai G2 20 S-TWIN with a LaB6 filament) using an accelerating voltage of 200 kV . The electrical and dielectric behaviors were studied by impedance spectroscopy in a wide frequency range ($40\text{--}10^7 \text{ Hz}$) by varying the applied temperature from 370 to 420 K with an Agilent 4294A analyzer.

3 Results and discussion

3.1 Structural properties

The crystal structure of the investigated compositions was examined by X-ray diffraction analysis. The powder XRD patterns of undoped ZnO and Fe/Al co-doped ZnO compositions are exhibited in Fig. 1.a. The structural characterization indicates that all the powdered samples have the hexagonal wurtzite structure according to the standard JCPDS file (card no. 36-1451) [4]. The XRD patterns of the co-doped $\text{Zn}_{0.94}\text{Fe}_{0.01}\text{Al}_{0.05}\text{O}$ nanoparticles shows the appearance of low intensity foreign peak (marked with *), which is attributed to the (1 1 1) reticular plane of face-centered-cubic Al metallic phase, according to JCPDS file 04-0787 [28]. For exploring more information of the Fe/Al co-doping effect on the structural properties of undoped ZnO, the enlarged XRD patterns of the most major peaks are presented in Fig. 1b. A shift of the intense diffraction peaks was observed by introduction of Fe and Al dopants into the ZnO host lattice. The shift in the peak position with Fe and Al addition proved the successful substitution of these dopants in the ZnO host matrix. On the other hand, this shift indicates a change of the structural parameters by the Fe/Al co-doping.

The structural parameters of the different investigated compositions were evaluated using the expressions:

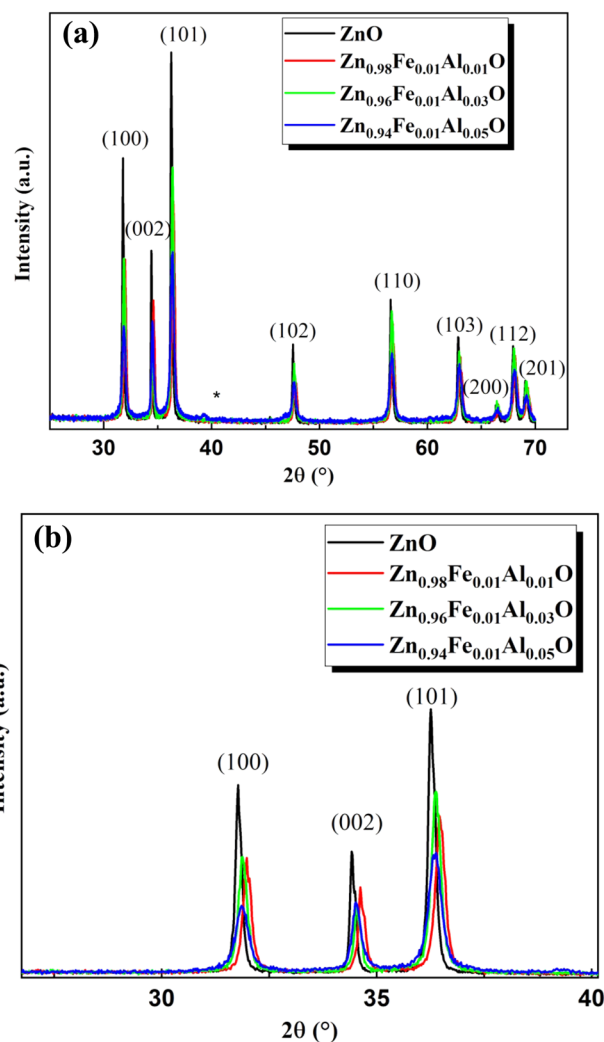


Fig. 1 a XRD patterns of undoped ZnO and co-doped $\text{Zn}_{(0.99-x)}\text{Fe}_{0.01}\text{Al}_x\text{O}$ ($x=0.01, 0.03$ and 0.05) compositions and b enlarged image of the more prominent diffraction peaks of all the experimented nanoparticles

$$a = \frac{\lambda}{\sqrt{3}\sin\theta_{(100)}} \quad (1)$$

$$c = \frac{\lambda}{\sin\theta_{(002)}} \quad (2)$$

$$V = \frac{\sqrt{3}a^2c}{2} \quad (3)$$

In these expressions, λ define the wavelength of the $\text{CuK}\alpha$ radiation (1.54056 \AA) and θ denotes the diffraction angle.

The determined values of the structural parameters for different compositions are gathered in Table 1. The lattice constants as well the unit cell volume expose decreasing trend

Table 1 Structural parameters of undoped ZnO, co-doped Zn_{0.98}Fe_{0.01}Al_{0.01}O, Zn_{0.96}Fe_{0.01}Al_{0.03}O and Zn_{0.94}Fe_{0.01}Al_{0.05}O nanoparticles

Nanopowders	<i>a</i> (Å)	<i>c</i> (Å)	<i>V</i> (Å ³)	<i>D</i> (nm)	ϵ	δ (line/nm ²)
ZnO	3.2518	5.2017	47.6347	45.21	0.0024	0.0004
Zn _{0.98} Fe _{0.01} Al _{0.01} O	3.2416	5.1946	47.2703	36.48	0.0032	0.0007
Zn _{0.96} Fe _{0.01} Al _{0.03} O	3.2423	5.1952	47.2962	28.63	0.0039	0.0012
Zn _{0.94} Fe _{0.01} Al _{0.05} O	3.2437	5.1963	47.3471	23.07	0.0048	0.0018

in the co-doped compositions as compared to undoped ZnO composition. The decreasing trend of the structural parameters can be explained by the smaller ionic radii of Fe³⁺ (0.064 nm) and Al³⁺ (0.054 nm) compared to Zn²⁺ (0.074 nm) [29]. The noted increase in the value of the structural parameters for the high doping concentration is possibly related to the Al secondary phase. Further, the structural parameters of co-doped samples demonstrate the efficient incorporation of Fe and Al in the ZnO lattice. The crystallite size in undoped and co-doped ZnO samples was determined using the Scherrer formula:

$$D = \frac{0.9\lambda}{\beta \cos\theta} \quad (4)$$

The dislocation density and the strain of the ZnO nanopowder samples were calculated by the following relations:

$$\delta = \frac{1}{D^2} \quad (5)$$

$$\epsilon = \frac{\beta}{4 \tan\theta} \quad (6)$$

In these expressions, λ represents the X-ray wavelength of the CuK α radiation (1.54056 Å), β denotes the full width at half maximum and θ defines the diffraction angle.

The calculated values of the crystallite size, dislocation density and strain for the different compositions are tabulated in Table 1. A decrease in the crystallite size was obtained with the elevation of Al co-doping concentration. The decrease of the crystallite size through Fe/Al co-doping is accompanied by the strain increase. This result proves the rise of the structural imperfections/defects, as induced by Fe/Al co-doping. The crystallite size reduction in the co-doped samples reveals that Fe or Al doping elements inhibit the growth of ZnO nanocrystals. Similar result was obtained for Fe/Al co-doped nanorods prepared by the hydrothermal process [25]. The crystallite size reduction can be explained by several effects: (1) the increase in the structural imperfections or defects through the Fe/Al addition into ZnO matrix, (2) effect of Zener pinning and (3) secondary phase formation which acts as grain growth inhibitor [4].

3.2 Morphological properties

Transmission Electron Microscope (TEM) technique was applied to further investigate the morphology, crystallite size

and shapes of the nanoparticles. The TEM micrographs of undoped and Fe/Al co-doped ZnO samples are presented in Fig. 2a–d. The morphology of undoped ZnO reveals the agglomeration of spherical nanoparticles with homogenous distribution. It is clearly noted from this image that the morphology is significantly

affected by the Al co-doping concentration. In fact, the TEM micrographs of Zn_{0.98}Fe_{0.01}Al_{0.01}O and Zn_{0.96}Fe_{0.01}Al_{0.03}O samples demonstrated that these co-doping percentage of Al (1% and 3%) did not change the morphology of ZnO nanostructures. Moreover, the agglomeration augmentation and the diminution size of almost nanoparticles were clearly observed with increasing Al co-doping concentration. Moreover, the agglomeration augmentation and the diminution size of almost nanoparticles were plainly observed with increasing Al co-doping concentration. The higher Al co-doping concentration alters the morphology of ZnO nanostructures. In fact, the morphology of Zn_{0.94}Fe_{0.01}Al_{0.05}O compositions reveals the formation of rod-like nanoparticles. In fact, the morphology of Zn_{0.94}Fe_{0.01}Al_{0.05}O compositions reveals the formation of rods nanoparticles. The morphology change obtained for the higher Al co-doping concentrations is probably related to the presence of the secondary phase. The SAED patterns of undoped and Zn_{0.94}Fe_{0.01}Al_{0.05}O nanopowders is indexed in Fig. 2e–f, which indicate the good crystallinity of the samples. This measurement reveals the presence of some additional set of diffraction rings for the higher Al co-doping concentration. These supplementary diffraction rings are indexed to (111), (200), (220), (311) and (222) planes of the secondary phase Al. TEM analysis suggests the efficient incorporation of Fe and Al dopants into the ZnO crystal lattice.

3.3 Vibrational properties

The Fourier transform infrared (FTIR) analysis was performed aiming to explore the presence of the chemical bondings and functional groups in the as-synthesized nanopowders. The FTIR spectra of undoped and co-doped ZnO compositions are depicted in Fig. 3. The characteristic mode corresponding to the stretching of Zn–O is located in the range of 520–560 cm⁻¹ for all the powdered compositions, as seen in the first enlarged image [400–750 cm⁻¹] [27]. This vibrational mode was observed for others compounds

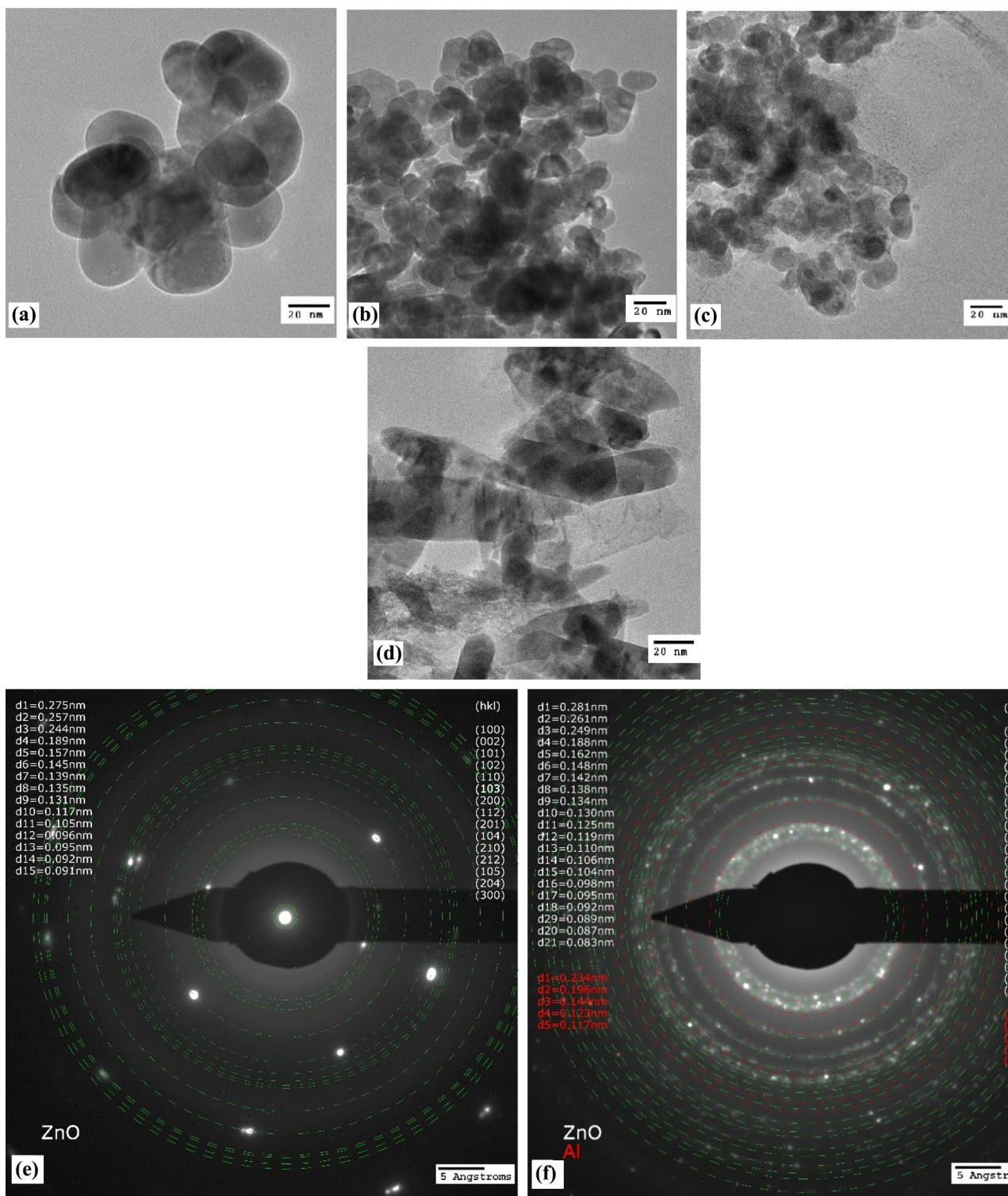


Fig. 2 TEM micrographs of undoped ZnO (a), co-doped Zn_{0.99}Fe_{0.01}Al_{0.01}O (b), co-doped Zn_{0.96}Fe_{0.01}Al_{0.03}O (c) and co-doped Zn_{0.94}Fe_{0.01}Al_{0.05}O nanoparticles (d). e Presents the (SAED) of undoped and f presents the (SAED) of co-doped ZnO (Zn_{0.94}Fe_{0.01}Al_{0.05}O)

based ZnO [30–32]. This characteristic absorption band is moved to the higher wavenumber domain due to Fe/Alco-doping. The slight shift of this vibrational mode is primarily

associated to the difference in the bond lengths caused by the replacement of these investigated dopants Fe and Al for Zn in the ZnO crystal lattice [4]. The FTIR spectra of Fe/Al

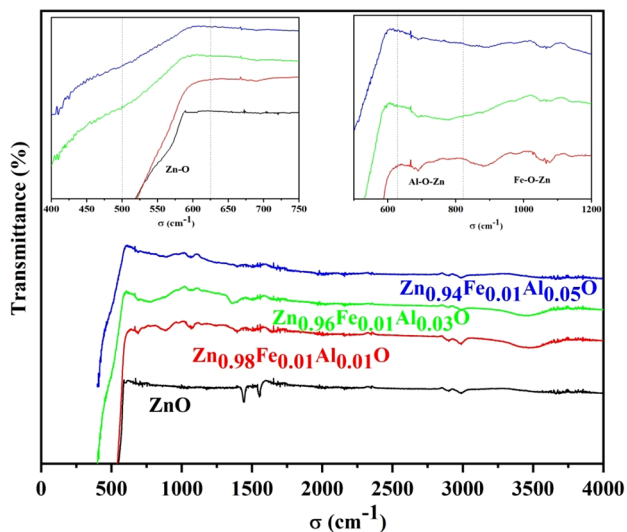


Fig. 3 FTIR spectra of undoped ZnO and co-doped $\text{Zn}_{(0.99-x)}\text{Fe}_{0.01}\text{Al}_x\text{O}$ ($x = 0.01, 0.03$ and 0.05) compositions

co-doped ZnO reveals a slight shift in the peak positions, which can probably be assigned to the small atomic masses of Fe and Al dopants as compared to that of Zn [18]. The peaks appeared in the range of $1300\text{--}1700\text{ cm}^{-1}$ is attributed to the O–H–O bending vibration. Furthermore, the band located at 3500 cm^{-1} individual to the O–H stretching vibration [33–36]. These modes are presumably attributed to the amount of water absorbed on the samples surface emanating from the laboratory atmosphere [37]. It is trustworthy to note that the intensity of this band is found to increase under the Fe/Al co-doping. This result is related to the decrease of the crystallite size with the rise of Al concentration [38]. For the co-doped nanopowders, the different peaks, appeared in the wavenumber range of $900\text{--}1120\text{ cm}^{-1}$, are attributed to the vibration of Zn–Fe–O local bond and deficiency states [39]. The new vibrational mode corresponding to the vibration of Al–O–Zn is found around 680 cm^{-1} , as seen in the second enlarged image [$650\text{--}1200\text{ cm}^{-1}$] [28]. Indeed, the presence of these particular modes (Zn–Fe–O and Al–O–Zn) proves the successful substitution of Zn^{2+} ions by Fe^{3+} and Al^{3+} ions into the ZnO lattice structure.

3.4 Optical properties

UV–Vis spectroscopy was applied in order to determinate the optical properties of undoped and Fe/Al co-doped ZnO samples. The UV–Vis absorption spectra are shown in Fig. 4.

The absorbance in metal oxide nanostructures depends on various factors, such as band gap energy, nanoparticle size, oxygen vacancies, impurity centers and deformities or defects present in the grain structure [4]. A strong absorption

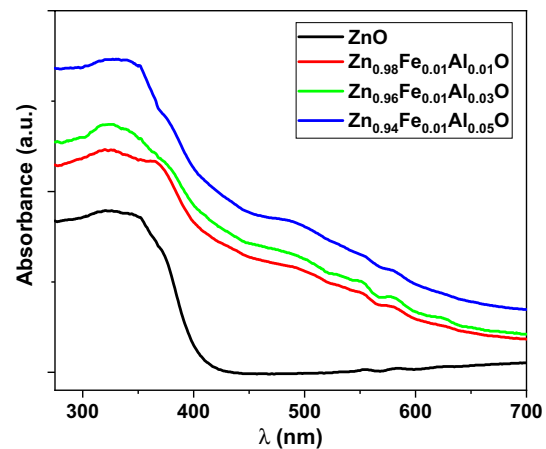


Fig. 4 Absorption spectra of undoped ZnO, $\text{Zn}_{0.98}\text{Fe}_{0.01}\text{Al}_{0.01}\text{O}$, $\text{Zn}_{0.96}\text{Fe}_{0.01}\text{Al}_{0.03}\text{O}$ and $\text{Zn}_{0.94}\text{Fe}_{0.01}\text{Al}_{0.05}\text{O}$ nanoparticles

peak around 385 nm was observed for all the powdered samples. In fact, the absorption peak located in the ultraviolet wavenumber range characterized the intrinsic absorption of ZnO nanostructures emerging from direct electronic transition (O_{2p} to Zn_{3d}) [4]. Further, some additional peaks in the visible wavenumber range, appeared precisely around 550 and 575 nm , were observed in the spectra of co-doped ZnO compositions. These peaks were attributed to the d–d transitions of Fe^{3+} ions [40]. A slight shift of these supplementary peaks with a diminution of intensity was noted with increasing Al co-doping concentration. These results prove the successful incorporation of Fe and Al dopants elements into the ZnO lattice crystal. Moreover, the absorbance of the prepared compositions in the visible wavenumber range rises with the increase of Al concentration. This effect is mostly attributed to the increase of the structural imperfections and defects created by co-doping [1]. Furthermore, the change in the absorption edge position along with the impurity addition in the ZnO host matrix indicates the band structure variation.

The optical band gap energy (E_g) is a fundamental parameter to figure out the utilization of semiconductors oxide materials in optoelectronic fields. The optical band gap energy of each composition was determined with the help of Tauc model:

$$(\alpha h\nu)^2 = A(E_g - h\nu) \quad (7)$$

In this model, α designates the optical absorption coefficient, A is a characteristic of the studied material and $(h\nu)$ signifies the photon energy. The optical band gap energy is obtained by extrapolating the vertical linear part of $(\alpha h\nu)^2$ versus $(h\nu)$, as shown in Fig. 5.

The deduced values for different compositions are depicted in Table 2. Co-doping with Fe and Al grounds a

prominent change of the optical band gap energy of ZnO nanostructures. The results show that the optical band gap energy decreased with Al co-doping concentration increase. The reduction of the optical properties obtained with increasing Al concentration can be interpreted by different effects. In fact, this diminution is likely to be related to the increase density of structural defects and imperfections or impurity states determined by DRX analysis [1, 2]. Consequently, such impurity band development create rise to new donor electronic states located just below ZnO conduction band due to hybridization of Al element in ZnO host matrix [25]. Second, the augmentation of the charge carrier concentration can be also another reason for the narrowing of the optical band gap energy obtained under Fe/Al co-doping effect [4]. The reduction in optical band gap energy may also be related to the formation

Table 2 Calculated values of band gap energy (E_g) and Urbach energy (E_u) of undoped ZnO, co-doped $\text{Zn}_{0.98}\text{Fe}_{0.01}\text{Al}_{0.01}\text{O}$, $\text{Zn}_{0.96}\text{Fe}_{0.01}\text{Al}_{0.03}\text{O}$ and $\text{Zn}_{0.94}\text{Fe}_{0.01}\text{Al}_{0.05}\text{O}$ nanoparticles

Nanopowders	E_g (eV)	E_u (eV)
ZnO	3.046	0.102
$\text{Zn}_{0.98}\text{Fe}_{0.01}\text{Al}_{0.01}\text{O}$	3.028	0.849
$\text{Zn}_{0.96}\text{Fe}_{0.01}\text{Al}_{0.03}\text{O}$	3.017	0.907
$\text{Zn}_{0.94}\text{Fe}_{0.01}\text{Al}_{0.05}\text{O}$	3.001	0.987

of the secondary phase at high Al concentrations [41]. In addition, the decrease of the optical band gap energy values is attributable to the s , p - d exchange interaction between the band electrons and the localized d electrons

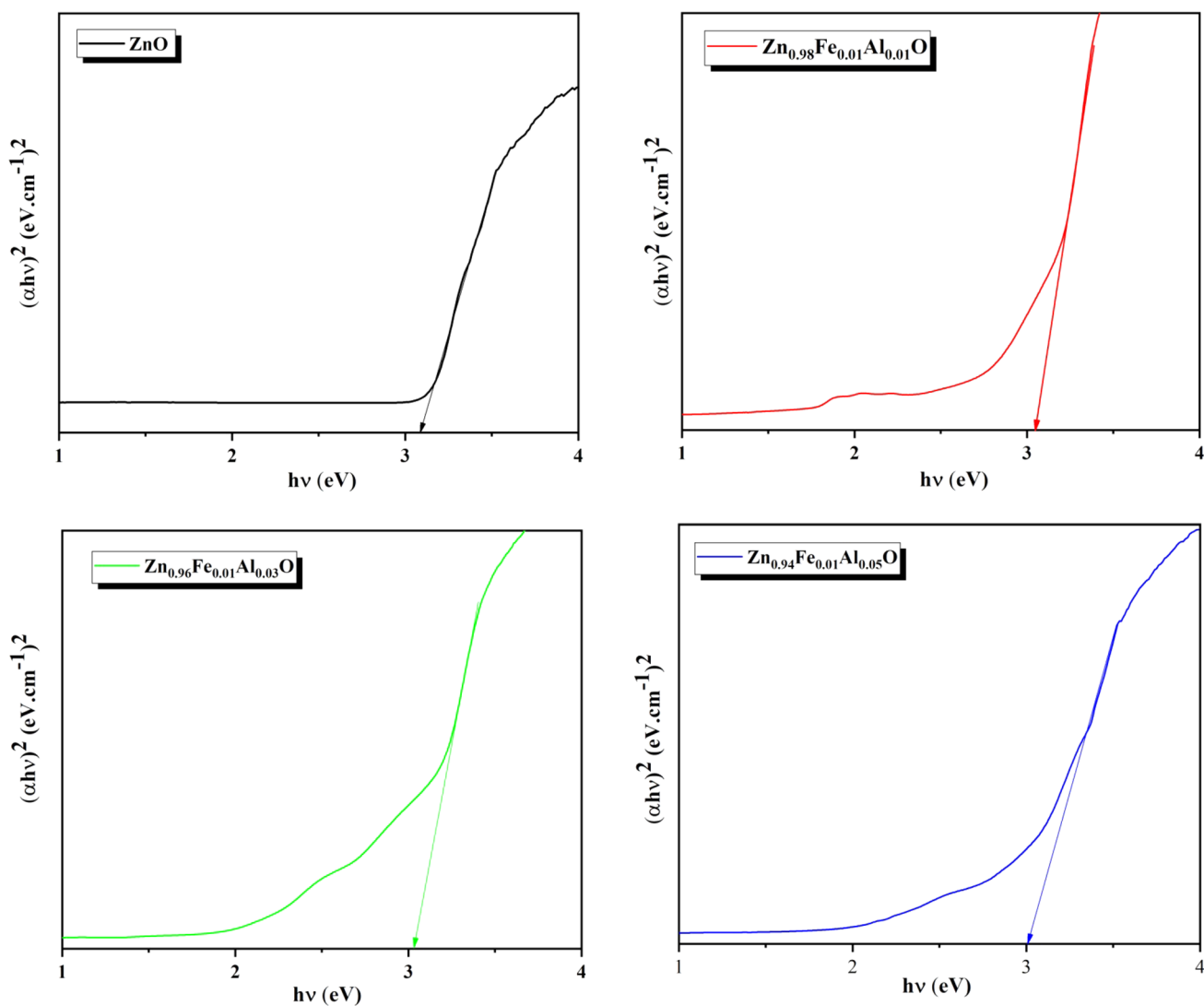


Fig. 5 Plots $(\alpha hv)^2$ versus photon energy (hv) for undoped ZnO and co-doped $\text{Zn}_{(0.99-x)}\text{Fe}_{0.01}\text{Al}_x\text{O}$ ($x=0.01, 0.03$ and 0.05) compositions

of the substituted co-doping elements [4]. These values are smaller than that obtained for others materials [42–44].

For more understanding the band structure of semi-conducting oxide materials, it would be comprehensive to pursue the band tailings in the adjacent of bands. Urbach energy (E_u) is an important parameter which measure the numerous disorders exist in the studied material [45].

The Urbach energy of undoped and Fe/Al co-doped ZnO at different concentration were correlated as the following expressions:

$$\ln(\alpha) = \ln(\alpha_0) + \frac{hv}{E_u} \quad (8)$$

Figure 6 represents the variation of $\ln(\alpha)$ versus (hv). The E_u values obtained for different compositions are reported in Table 2. This result confirms that Fe/Al co-doping increased the formation of imperfections and defects in the crystal lattice of ZnO. The highest value of Urbach energy obtained for $\text{Zn}_{0.94}\text{Fe}_{0.01}\text{Al}_{0.05}\text{O}$ indicates the formation of more interbands in between conduction and valence bands. As obviously seen in Fig. 7, the variation of the Urbach energy as a function of Al concentration was strongly correlates with structural disorder. This result confirms that Fe/Al co-doping effect increased the formation of more imperfections and defects in the lattice crystal of ZnO.

3.5 Impedance spectroscopy

For more comprehension the impact of Fe and Al co-doping effect on the electrical and dielectric properties of ZnO nanopowders: complex impedance, electric modulus, Ac

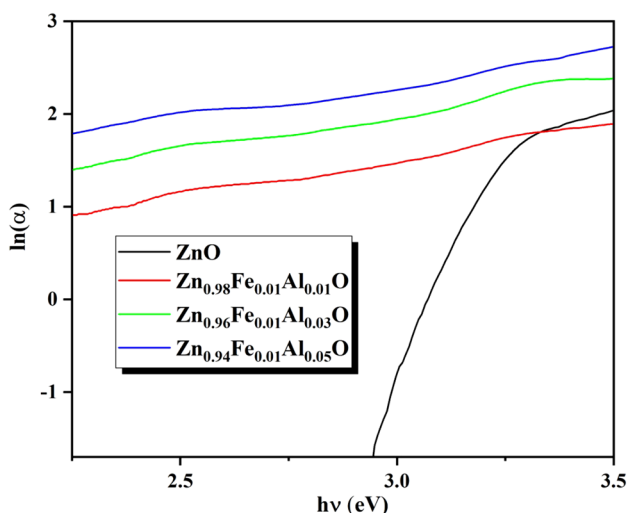


Fig. 6 Plots $\ln(\alpha)$ versus photon energy (hv) for undoped ZnO and co-doped $\text{Zn}_{(0.99-x)}\text{Fe}_{0.01}\text{Al}_x\text{O}$ ($x=0.01, 0.03$ and 0.05) compositions

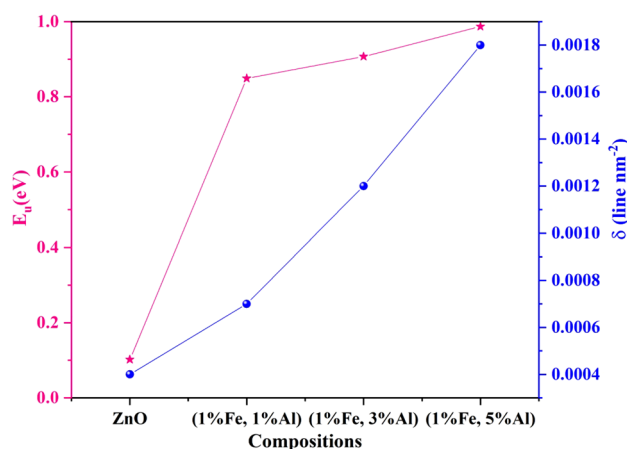


Fig. 7 Variation of Urbach energy and dislocation density as a function of compositions

conductivity, complex dielectric constant and loss tangent were investigated in our study.

3.5.1 Electrical properties

3.5.1.1 Impedance spectra The complex impedance spectroscopy is a perfect technique to explore the electrical properties of the investigated compounds. This method is based on analyzing the response of a perturbed system to an external electromagnetic excitation over a wide range of temperature and frequency. The Nyquist plots of undoped ZnO composition measured in temperature range [370–420 K] are depicted in Fig. 8. The same behavior was obtained for the others Fe/Alco-doped ZnO samples. The obtained spectra reveal the appearance of semicircular arcs, which diameter gradually decreases with the temperature increase. This result proves the semiconducting compartment of the studied composition [24, 46]. In addition, the center of these observed arcs is found to shift towards the lower resistance value with augmenting the operated temperature. Their centers are localized below the real part of the impedance, suggesting the non-Debye type of relaxation behavior in the studied composition [47, 48]. The comparative Nyquist plots of the different samples at selected temperature 380 K is presented in the inset of Fig. 8. It is clearly noted from this variation that the impedance is found to decline with increasing Al co-doping concentration in ZnO nanopowders.

The variation of the real part Z' of complex impedance for undoped ZnO composition is disclosed in Fig. 9. This variation indicates that the value of Z' decreases gradually with increasing frequency and then becomes nearly invariable in higher frequency range.

The decrease of Z' value with augmenting the frequency and operated temperature affirms the semiconducting

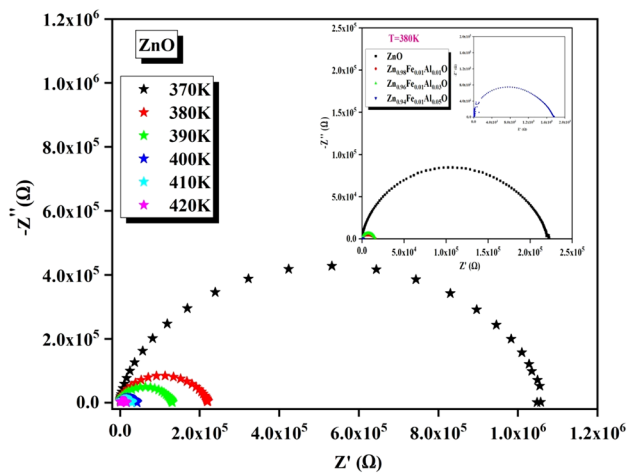


Fig. 8 Complex impedance spectra (Nyquist plot) of undoped ZnO nanoparticles at different temperatures. The inset presents the comparative Cole–Cole plots of all the experimented nanoparticles at 380 K

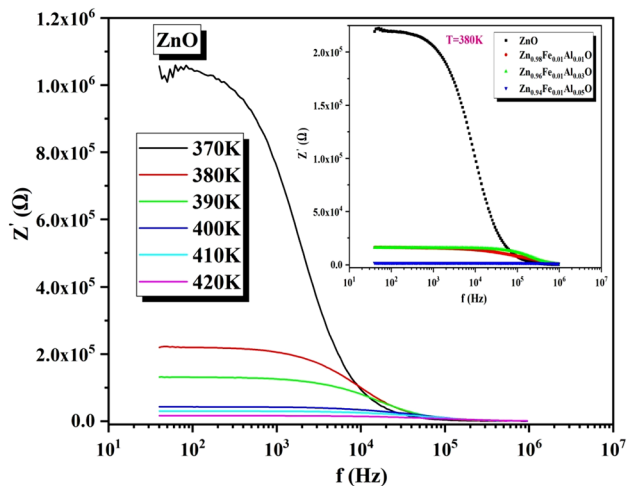


Fig. 9 Variation of real part of the impedance Z' with frequency at various temperatures for undoped ZnO nanoparticles. The inset presents the comparative variation of real part of the impedance Z' of all the experimented nanoparticles at 380 K

behavior of the studied samples [49]. It is clearly noted from this variation that the value of Z' emerges for all the operated temperature at higher frequencies. This observation is due to the release of space charge because of the reducing in the barrier properties [50, 51]. The magnitude of the real part of the complex impedance is found to decrease with the increase in Al concentration in ZnO, as obviously observed in the inset of Fig. 9.

The frequency dependance of the imaginary part Z'' of complex impedance for undoped ZnO at different temperatures is presented in Fig. 10. The obtained spectra

reveal the appearance of a single maximum peak Z''_{max} at particular frequency f_{max} defined the relaxation frequency.

The comparative evolution for the different compositions, presented in the inset of Fig. 10, shows that the magnitude decreases with augmenting Al co-doping concentration. This result is related by the decrement of the resistive part of the prepared compositions [24].

3.5.1.2 Frequency and temperature dependance of AC conductivity The electrical conductivity of undoped and co-doped ZnO nanopowder was evaluated using the expression that follows [24]:

$$\sigma_{tot} = \frac{e}{s} \times \frac{Z'}{Z'^2 + Z''^2} \tag{9}$$

where s designates the cross-sectional area of the deposited electrode and e denotes the pellet thickness.

The evolution of electrical conductivity as a function of frequency at selected temperatures in the undoped ZnO sample is displayed in Fig. 11. Similar behavior was also obtained for the co-doped ZnO compositions. This evolution reveals that the electrical conductivity drastically increases with the rise in frequency and operated temperature. The augmentation of the electrical conductivity with frequency is predominantly due to the increment in electron migration [52]. The elevation of the conductivity is probably assigned to the variable range-hopping mechanism of conduction [53]. The gradual increment of electrical conductivity with frequency could be understood in the light of Maxwell–Wagner model for the homogenous double structure.

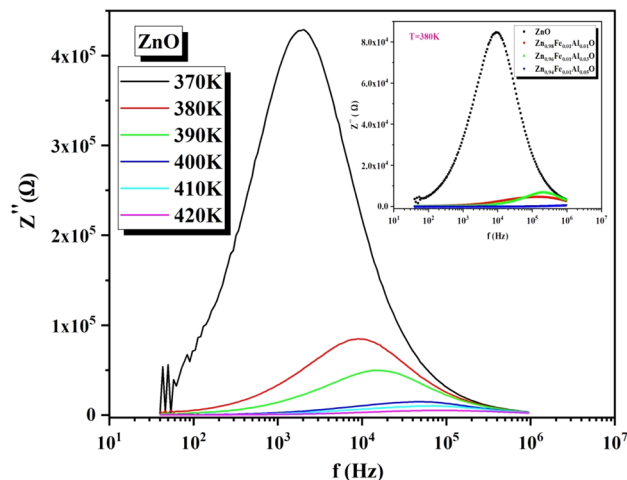


Fig. 10 Variation of imaginary part of the impedance Z'' along with frequency at various temperatures for undoped ZnO nanoparticles. The inset presents the comparative variation of imaginary part of the impedance Z'' of all the experimented nanoparticles at 380 K

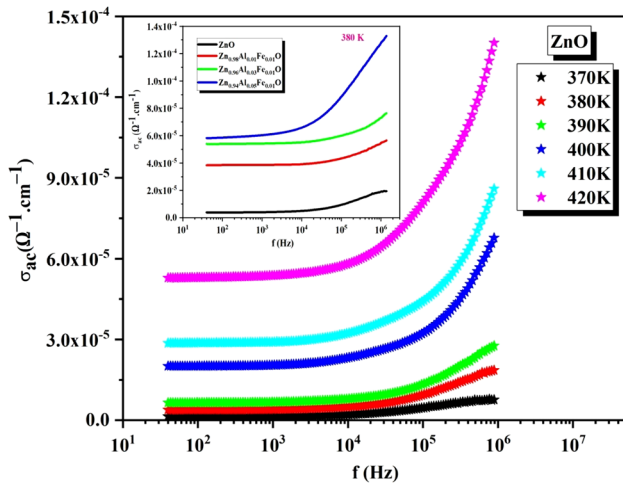


Fig. 11 Variation of AC conductivity along with frequency at various temperatures for undoped ZnO nanoparticles. The inset presents the comparative variation of AC conductivity of all the experimented nanoparticles at 380 K

In fact, the interfaces behave as a poorly conducting obstruction because of the development of microstructural defects which constrains the jumping frequency of free carriers [12]. Consequently, the free charge carriers behave like particles in a box [54].

At lower frequency region, the nominal increase in conductivity is due to the few charge carriers that cross the potential barrier. This movement produces a feeble rise conductivity [55]. With increasing the electric field frequency, the charge carriers get sufficient energy to cross the potential barrier resulting in electrical conductivity increase.

The comparative evolution of the electrical conductivity for the different compositions at fixed temperature is presented in the inset of Fig. 11. This evolution reveals that Fe/Al co-doping effect improves the electrical conductivity of ZnO nanopowders. This augmentation was mostly attributed to the rise concentration of charge carriers induced by the Al addition into ZnO crystal lattice [56]. The increment of the electrical conductivity was due to the decrease in hopping length as a result of Fe/Al co-doping in ZnO host matrix [57]. Further, the elevated value of the electrical conductivity obtained for the higher Al concentration was probably related to the existence of the secondary phase detected by DRX analysis. Similar result was also reported by other research work [58]. These obtained findings demonstrate that the co-doped ZnO nanopowders could be potential candidates for high-energy storage devices.

3.5.2 Dielectric properties

3.5.2.1 Dielectric constant Generally, the response of any dielectric material is determined by numerous aspects such

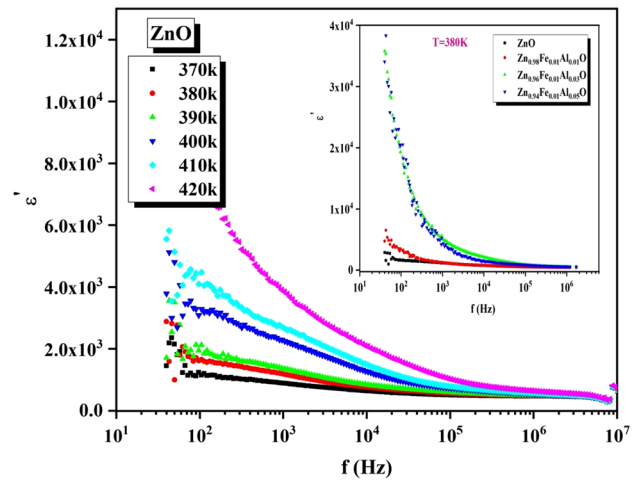


Fig. 12 Variation of dielectric constant along with frequency at various temperatures for undoped ZnO nanoparticles. The inset presents the comparative variation of dielectric constant of all the experimented nanoparticles at 380 K

as applied electric field frequency, structural imperfections or defects, morphology and size of the grains and chemical defects etc. The dielectric response is defined by the following expressions:

$$\epsilon^* = \epsilon' + j\epsilon'' \tag{10}$$

$$\epsilon' = \frac{Z'}{\omega C_0(Z'^2 + Z''^2)} \tag{11}$$

$$\epsilon'' = \frac{Z''}{\omega C_0(Z'^2 + Z''^2)} \tag{12}$$

In these relations, ϵ' and ϵ'' represent the real and the imaginary parts of the dielectric constant, which designates the stored and dissipated energy, respectively. C_0 symbolizes the vacuum capacitance of the cell.

Several factors can strongly influence the dielectric characteristics, like frequency of external electric field, sintering temperature, microstructure, defect's concentration (oxygen vacancies and zinc interstitials), type of cation substitution, etc. [31]. The frequency dependence of the dielectric constant for the undoped ZnO composition at several temperatures is depicted in Fig. 12. The same behavior was also obtained for the co-doped $Zn_{0.98}Fe_{0.01}Al_{0.01}O$, $Zn_{0.96}Fe_{0.01}Al_{0.03}O$ and $Zn_{0.94}Fe_{0.01}Al_{0.05}O$ samples. This variation reveals that the dielectric constant is strongly affected by the operated temperature and frequency of the electrical field. In fact, its value is found to decline with frequency and rise with temperature. This type of evolution could be understood in the light of the dielectric relaxation

phenomenon inside dielectric oxide nanomaterials. The Koop phenomenological theory and Maxwell–Wagner interfacial model can be used to explain the observed dispersion of the dielectric constant for our investigated compositions [30, 59–61]. In this theory, the dielectric material has a homogeneous double structure. In fact, the highly conducting grains are separated by the highly resistive grain boundaries. In applied electric field, carriers can migrate over the grain bulk and are accumulated at the insulating grain boundaries [62]. This process involves large polarization characterized by an elevated value of dielectric constant at the lower frequency domain. Moreover, the augmented value of ϵ' is correlated to the collective contribution of all type of polarization like ionic, electronic, interfacial and dipolar [46, 58]. At higher frequencies, two type of polarizations (orientational and space charge polarizations) are vanished and only electronic and ionic polarizations are active resulting in small value of ϵ' [58]. In addition, some different aspects can be interpreted the higher value of the dielectric constant at low frequencies such as: (1) the lower conductivity on the surface of grain, (2) the ionic polarization and (3) the effect of oxygen vacancies, grain boundary defects and dangling bond [12]. Furthermore, the decrease of dielectric constant with frequency increase is strongly combine with the polarizability loss of some species. In fact, the carrier hopping is incapable to pursue the fast variation of the external electric field at elevated frequencies [19]. Whereas, the increase of dielectric constant with temperature is attributed to the thermal motion of molecules. The comparative variation of the dielectric constant of all samples is presented in the inset of Fig. 12. It is still noticeable that the value of ϵ' increases gradually with the increase of Al concentration. This figure proves that Al addition improves the dielectric constant of ZnO nanopowders. The improvement of dielectric constant of ZnO with Fe/Al co-doping can be understood in the light of numerous factors: first, Al incorporation into ZnO crystal lattice introduces new charge carriers into the co-doped compound [63]. Second, the reduction in crystalline size, noted under Fe and Al addition, can be other effect that contributes to the ϵ' increment. Similar result was also obtained by others works [64, 65]. Third, the enhancement of dielectric constant with Fe/Al co-doping can be attributed to the large dielectric polarizability of Fe and Al ions compared with Zn ions [66].

3.5.2.2 Dielectric loss Frequency dependence of the dielectric loss ($\tan\delta = \frac{\epsilon''}{\epsilon'}$) of undoped ZnO sample at selected temperatures is presented in Fig. 13. Similar evolution was also obtained for the co-doped $\text{Zn}_{0.98}\text{Fe}_{0.01}\text{Al}_{0.01}\text{O}$, $\text{Zn}_{0.96}\text{Fe}_{0.01}\text{Al}_{0.03}\text{O}$ and $\text{Zn}_{0.94}\text{Fe}_{0.01}\text{Al}_{0.05}\text{O}$ samples. As obvi-

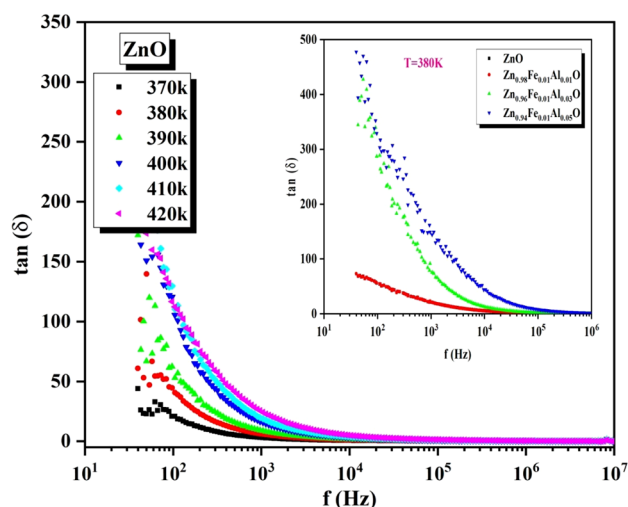


Fig. 13 Variation of dielectric loss along with frequency at various temperatures for undoped ZnO nanoparticles. The inset present the comparative variation of dielectric loss of all the experimented nanoparticles at 380 K

ously observed in the inset of Fig. 13, the dielectric loss decreases continuously with frequency indicating the usual dispersion behavior. At lower frequency domain, the augmented value of dielectric loss is related to the impurity introduction, crystal defects and moisture existed in the studied samples [12]. Further, the inflated value of the dielectric loss noted at lower frequencies and higher operated temperature is due to the space charge polarization. The Shockley–Read mechanism can be used to interpret this effect [65]. In fact, the capturing of surface electrons by the impurity ion introduced in the bulk crystal matrices is the source of the space charge polarization responsible for the elevated value at lower frequencies and at higher temperatures [67]. This process rises with the elevation of temperature, which tends to augment the value of the dielectric loss. In addition, another aspect that contribute to the highest value of the dielectric loss at higher temperatures is probably due to conduction loss. In fact, the movement of ions over large distance led to loss of electric energy as amount of their energy are converted to the lattice as heat energy. With temperature rise, the conduction loss becomes higher due to the rise of the ion mobility. This effect introduces the increase of the dielectric loss at higher temperatures [46]. The comparative variation of the dielectric loss for the different compositions at fixed temperature 380 K is presented in the inset of Fig. 13. The increment of the dielectric loss with Fe/Al incorporation into ZnO crystal lattice is associated to the increase of the defect's concentration (oxygen vacancies and zinc interstitials) presented in the co-doped compositions [24].

3.5.3 Modulus analysis

Actually, the electrical modulus formalism is extensively applied for investigating the electrical relaxation phenomena. This analysis provides insights to the conduction mechanism and relaxation processes by eliminating the effect of electrode polarization in the lower frequency range. To study the type of the conduction processes (localized or non-localized), the comparison of modulus and impedance data of the prepared compositions are presented in Fig. 14. This figure reveals that Fe/Al co-doping effect did not change the non-Debye behavior and suggests the presence of a short-range movement of charge carriers of ZnO powdered compositions [68]. As seen in Fig. 15, the comparative variation of M'' at selected temperature 380 K reveals that the magnitude of the maximum peak was significantly affected by Fe and Al addition into ZnO host matrix and the peak position was moved towards the higher frequency. This result combines

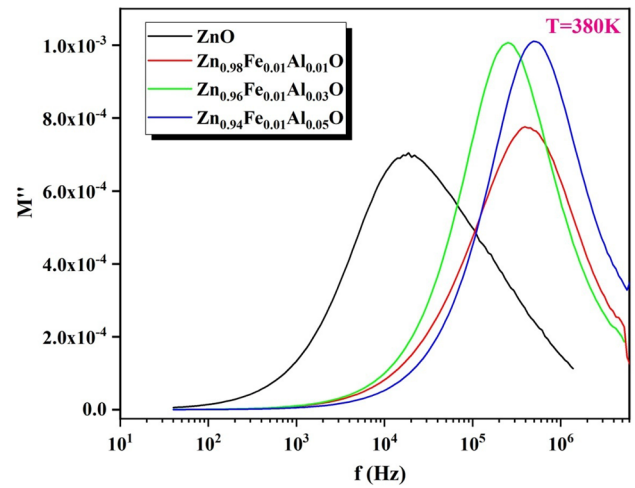


Fig. 15 Variation of imaginary part of the modulus M'' along with frequency at various temperatures for all the compositions

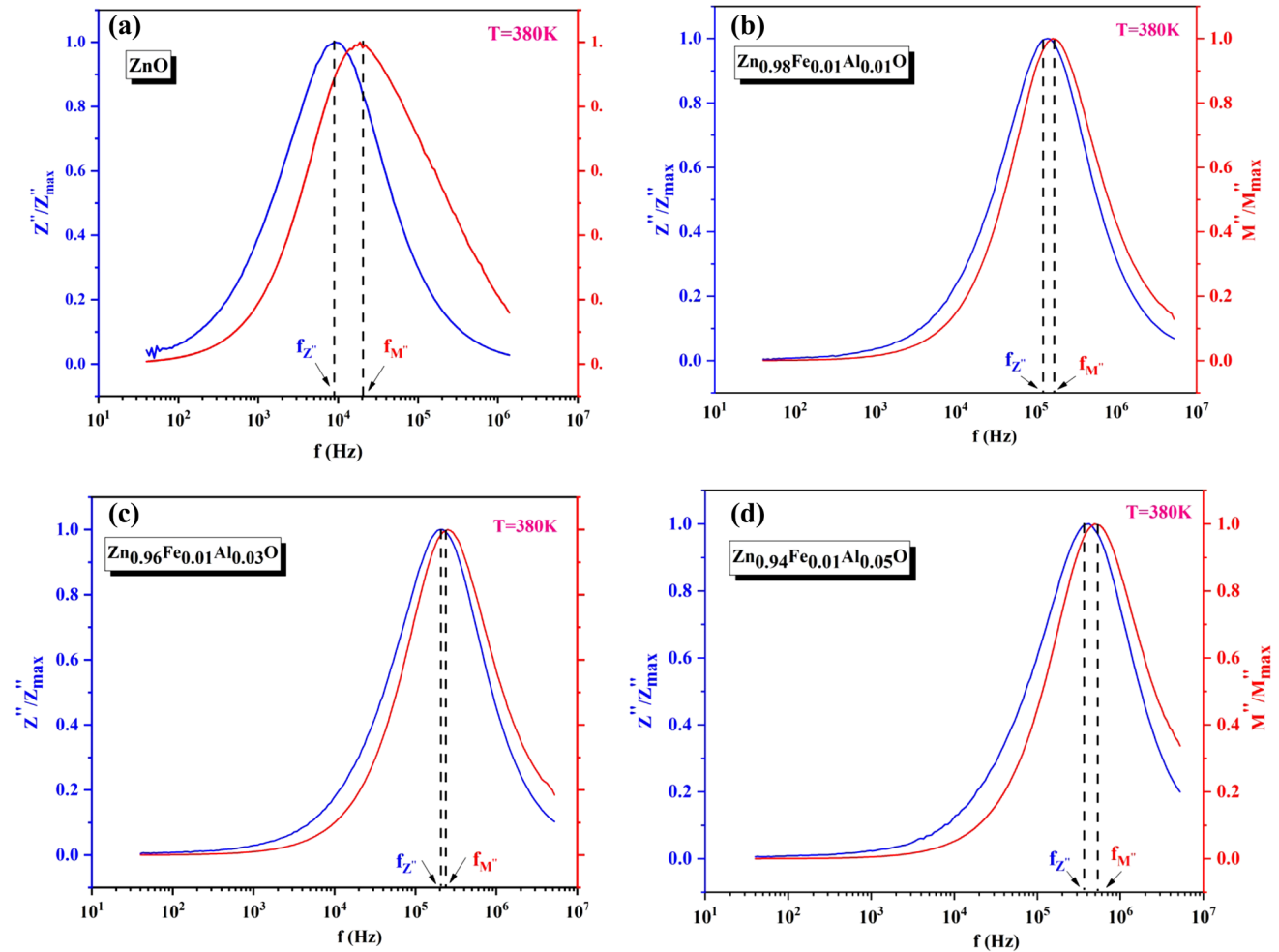


Fig. 14 Frequency dependence of normalized peaks M''/M''_{max} and Z'/Z''_{max} of undoped ZnO (a) and co-doped $Zn_{(0.99-x)}Fe_{0.01}Al_xO$ [$x=0.01$ (b), 0.03 (c) and 0.05 (d)] compositions

strongly with the microstructure development and also to the existence of a distribution of relaxation time.

4 Conclusion

The undoped and Fe/Al co-doped ZnO nanopowder samples at different Al co-doping concentrations (1, 3 and 5%) were efficiently synthesized through the co-precipitation method. The structural, vibrational, optical, morphological, electrical and dielectric properties of the ZnO-based compounds were well investigated through various complementary characterizations. The structural analysis revealed that the Fe/Al co-doping in ZnO crystal lattice did not change the hexagonal structure of the matrix. The FTIR analysis showed the presence of Zn–Fe–O and Al–O–Zn vibrational modes for the co-doped ZnO compositions, affirming the successful incorporation of dopants elements into ZnO host matrix.

The morphological study suggested that the morphology of ZnO was strongly influenced by the Al co-doping concentration. This measurement revealed the formation of spherical nanoparticles for undoped ZnO nanostructures and their average size was clearly reduced by the introduction of Al ions. Whereas, the morphology changed to rod shapes at higher Al co-doping concentrations. Further, the optical study showed the presence of additional absorption peaks in the visible range corresponding to the $d-d$ transition of Fe^{3+} ions in the co-doped ZnO compositions. These absorption peaks moved towards higher wavenumbers with increasing the Al co-doping concentration. The absorption measurements demonstrated that the band gap energy gradually decreased with increasing Al co-doping concentration. The Urbach energy was found to increase under the Fe/Al co-doping effect. Moreover, the electrical properties proved the semiconducting compartment of all the powdered samples. The electrical conductivity was found to increase under Fe and Al introduction into ZnO lattice structure thanks to Al element. The improvement of the optical and electrical properties obtained for the Fe/Al co-doped ZnO compositions make them suitable for optoelectronic devices.

Acknowledgements The authors gratefully acknowledge the financial support of DGRST. They would like to thank Prof. Ali Khalfallah (University of Coimbra) and Prof. Maria Teresa Vieira (University of Coimbra) for their helpful contribution in this work.

Author contribution statement HS: methodology, investigation, writing–original draft, writing–review and editing. ZB: conceptualization, methodology, investigation, supervision, writing–original draft, writing–review and editing. PS: methodology. YH: methodology. DM: methodology. KK: methodology. NA: resources. HK: resources.

Data availability The raw/processed data required to reproduce these findings cannot be shared at this time as the data also form a part of an ongoing study.

Declarations

Conflict of interest The authors declare that they have no known competing financial interests or personal relationships that could have appeared to influence the work reported in this paper.

References

1. J. Singh, R.C. Singh, Enhancement of optical, dielectric and transport properties of (Sm, V) co-doped ZnO system and structure-property correlations. *Ceram. Int.* **47**, 10611–10627 (2021)
2. R. Vettumperumal, S. Kalyanaraman, B. Santoshkumar, R. Thangavel, Estimation of electron-phonon coupling and Urbach energy in group-I elements doped ZnO nanoparticles and thin films by sol–gel method. *Mater. Res. Bull.* **77**, 101–110 (2016)
3. B. Dey, R. Narzary, L. Chouhan, S. Bhattacharjee, B.N. Parida, A. Mondal, S. Ravi, S.K. Srivastava, Crystal structure, optical and dielectric properties of Ag:ZnO composite-like compounds. *J Mater Sci: Mater Electron.* **33**, 2855–3286 (2022)
4. H. Saadi, F.I.H. Rhouma, Z. Benzarti, Z. Bougrioua, S. Guerhazi, K. Khirouni, Electrical conductivity improvement of Fe doped ZnO nanopowders. *Mater. Res. Bull.* **129**, 110884–110895 (2020)
5. C.V. Ramana, S. Utsunomiya, R.C. Ewing, U. Becker, V.V. Atuchin, V.Sh. Aliev, V.N. Kruchinin, Spectroscopic ellipsometry characterization of the optical properties and thermal stability of ZrO_2 films made by ion-beam assisted deposition. *Appl. Phys. Lett.* **92**, 011917–011920 (2008)
6. V.A. Shvets, V.Sh. Aliev, D.V. Gritsenko, S.S. Shaimeev, E.V. Fedosenko, S.V. Rykhliiski, V.V. Atuchin, V.A. Gritsenko, V.M. Tapilin, H. Wong, Electronic structure and charge transport properties of amorphous Ta_2O_5 . *J. Non-Cryst. Solids* **354**, 3025–3033 (2008)
7. N.N. Golovnev, M.S. Molkeev, I.V. Sterkhova, M.K. Lesnikov, V.V. Atuchin, Coordination effects in hydrated manganese (II) 1,3-diethyl-2-thiobarbiturates and their thermal stability. *Polyhedron* **134**, 120–125 (2017)
8. L. Dyshlyuk, O. Babich, S. Ivanova, N. Vasilchenko, V. Atuchin, I. Korolkov, D. Russakov, A. Prosekov, Antimicrobial potential of ZnO, TiO_2 and SiO_2 nanoparticles in protecting building materials from biodegradation. *Int. Biodeterior. Biodegrad.* **146**, 104821–104828 (2020)
9. V.V. Atuchin, M.S. Lebedev, I.V. Korolkov, V.N. Kruchinin, E.A. Maksimovskii, S.V. Trubin, Composition-sensitive growth kinetics and dispersive optical properties of thin $\text{Hf}_x\text{Ti}_{1-x}\text{O}_2$ ($0 \leq x \leq 1$) films prepared by the ALD method. *J. Mater. Sci.: Mater. Electron.* **30**, 812–823 (2019)
10. A.M. El Nahrawy, A.B.A. Hammad, A.M. Mansour, Structural investigation and optical properties of Fe, Al, Si, and Cu– ZnTiO_3 nanocrystals. *Phys. Scr.* **96**, 115801 (2021)
11. A.B.A. Hammad, A.M. Mansour, A.M. El Nahrawy, Ni^{2+} doping effect on potassium barium titanate nanoparticles: enhancement optical and dielectric properties. *Phys. Scr.* **96**, 125821 (2021)
12. M. Kaur, V. Kumar, P. Kaur, M. Lal, P. Negi, R. Sharma, Effect on the dielectric properties due to In–N co-doping in ZnO particles. *J. Mater. Sci: Mater Electron.* **32**, 8991–9004 (2021)

13. B. Poornaprakash, S. Ramu, K. Subramanyam, Y.L. Kim, M. Kumar, M.S.P. Reddy, Robust ferromagnetism of ZnO:(Ni+Er) diluted magnetic semiconductor nanoparticles for spintronic applications. *Ceram. Int.* **47**, 18557–18564 (2021)
14. P. Sahoo, A. Sharma, S. Padhan, G. Udayabhanu, R. Thangavel, UV-assisted water splitting of stable Cl-doped ZnO nanorod photoanodes grown via facile sol–gel hydrothermal technique for enhanced solar energy harvesting applications. *Sol. Energy* **193**, 148–216 (2019)
15. U. Alam, A. Khan, D. Ali, D. Bahnemann, M. Muneer, Comparative photocatalytic activity of sol–gel derived rare earth metal (La, Nd, Sm and Dy) doped ZnO photocatalysts for degradation of dyes. *RSC Adv.* **8**, 17582–17594 (2018)
16. B.L. da Silva, B.L. Caetano, B.G. Chiari-Andreo, R.C.L.R. Pietro, L.A. Chiavacci, *Colloids Surf. B: Biointerfaces.* **177**, 440–447 (2019)
17. N.A. Shad, M.M. Sajid, Y. Javed, N. Amin, M. Ikram, K. Akhtar, G. Ahmad, F. Ali, A. Razaq, High-yield synthesis of pure ZnO nanoparticles by one-step solid-state reaction approach for enhanced photocatalytic activity. *J. Chin. Chem. Soc.* **67**, 1045–1053 (2020)
18. F. Kabir, A. Murtaza, A. Saeed, A. Ghani, A. Ali, S. Khan, L. Kaili, Z. Qizhong, Y.K. Kang, S. Yang, Room temperature ferromagnetism in dilute magnetic semiconducting ZnO nanoparticles co-doped with Tb and Fe. *J Mater Sci: Mater Electron.* **32**, 10734–11074 (2021)
19. W. Bouslama, M.B. Ali, N. Sdiri, H. Elhouichet, Conduction mechanisms and dielectric constant features of Fe doped ZnO nanocrystals. *Ceram. Int.* **47**, 19106–19114 (2021)
20. P.R. Chithira, T.T. John, Correlation among oxygen vacancy and doping concentration in controlling the properties of cobalt doped ZnO nanoparticles. *J. Magn. Magn. Mater.* **496**, 165928–165959 (2020)
21. M.S. Nadeem, T. Munawar, F. Mukhtar, M.N. Rahman, M. Riaz, F. Iqbal, Enhancement in the photocatalytic and antimicrobial properties of ZnO nanoparticles by structural variations and energy bandgap tuning through Fe and Co co-doping. *Ceram. Int.* **47**, 11109–11121 (2021)
22. T.M. Bawazeer, M.S. Alsoufi, M. Shkir, B.M. Al-Shehri, M.S. Hamdy, Excellent improvement in photocatalytic nature of ZnO nanoparticles via Fe doping content. *Inorg. Chem. Commun.* **130**, 108668–108691 (2021)
23. R. Selvanayak, M. Rameshbabu, S. Muthupandi, M. Razia, S.S. Florence, K. Ravichandran, K. Prabha, Structural, optical and electrical conductivity studies of pure and Fe doped Zinc Oxide (ZnO) nanoparticles. *Mater. Today: Proc.* **497**, 2628–2631 (2022)
24. H. Saadi, Z. Benzarti, F.I.H. Rhouma, P. Sanguino, S. Guermazi, K. Khirouni, M.T. Vieira, Enhancing the electrical and dielectric properties of ZnO nanoparticles through Fe doping for electric storage applications. *J. Mater. Sci. Mater. Electron.* **32**, 1536–1556 (2021)
25. N.R. Khalid, A. Hammad, M.B. Tahir, M. Rafique, T. Iqbal, G. Nabi, M.K. Hussain, Enhanced photocatalytic activity of Al and Fe co-doped ZnO nanorods for methylene blue degradation. *Ceram. Int.* **45**, 21430–21435 (2019)
26. M.U. Tariq, Y. Li, W.-X. Li, Z.-R. Yu, J.-M. Li, Y.-M. Hu, M.-Y. Zhu, H.-M. Jin, Y. Liu, Y.-B. Li, K. Skotnicova, Structural, ferromagnetic, and optical properties of Fe and Al co-doped ZnO diluted magnetic semiconductor nanoparticles synthesized under high magnetic field. *Adv. Manuf.* **7**, 248–255 (2019)
27. M. Jannesari, M. Asemi, M. Ghanaatshoar, Sol–gel preparation of Fe and Al co-doped ZnO nanostructured materials. *J Sol-Gel Sci Technol.* **83**, 181–189 (2017)
28. P.G. Ray, M. Das, M. Wan, C. Jacob, S. Roy, P. Basak, S. Dhara, Surfactant and catalyst free facile synthesis of Al-doped ZnO nanorods—an approach towards fabrication of single nanorod electrical devices. *Appl. Surf. Sci.* **512**, 145732–145739 (2020)
29. M. Tariq, Y. Li, W.-X. Li, Z.-R. Yu, J.-M. Li, Y.-M. Hu, M.-Y. Zhu, H.-M. Jin, Y. Liu, Y.-B. Li, K. Skotnicova, Structural, ferromagnetic, and optical properties of Fe and Al co-doped ZnO diluted magnetic semiconductor nanoparticles synthesized under high magnetic field. *Adv. Manuf.* **7**, 248–255 (2019)
30. A.M. El Nahrawy, A.B.A. Hammad, A.M. Bakr, Th.I. Shaheen, A.M. Mansour, Sol–gel synthesis and physical characterization of high impact polystyrene nanocomposites based on Fe₂O₃ doped with ZnO. *Appl. Phys. A.* **126**, 654–664 (2020)
31. A.M. El Nahrawy, A.S. Montaser, A.M. Bakr, A.B.A. Hammad, A.M. Mansour, Impact of ZnO on the spectroscopic, mechanical, and UPF properties of Fe₂O₃-tough polystyrene-based nanocomposites. *J Mater Sci: Mater Electron.* **32**, 28019–28031 (2021)
32. A. Dahshan, A.B.A. Hammad, K.A. Aly, A.M. El Nahrawy, Eu₂O₃ role in the optical and photoluminescence properties of 50SiO₂-7 MgO-20 ZnO-(23-x) La₂O₃ - x Eu₂O₃ nano-crystalline thin film. *Appl. Phys. A.* **126**, 19–26 (2020)
33. H. Ji, Z. Huang, Z. Xia, M.S. Molokeev, X. Jiang, Z. Line, V.V. Atuchin, Comparative investigations of the crystal structure and photoluminescence property of eulytite-type Ba₃Eu(PO₄)₃ and Sr₃Eu(PO₄)₃. *Dalton Trans.* **44**, 7679–86 (2015)
34. V.V. Atuchin, A.K. Subanakov, A.S. Aleksandrovsky, B.G. Bazarov, J.G. Bazarova, S.G. Dorzhieva, T.A. Gavrilova, A.S. Krylov, M.S. Molokeev, A.S. Oreshonkov, A.M. Pugachev, Yu.L. Tushinova, A.P. Yelissev, Exploration of structural, thermal, vibrational and spectroscopic properties of new noncentrosymmetric double borate Rb₃NdB₆O₁₂. *Adv. Powder Technol.* **28**, 1309–1315 (2017)
35. V.V. Atuchin, L.I. Isaenko, V.G. Kesler, Z.S. Lin, M.S. Molokeev, A.P. Yelissev, S.A. Zhurkov, Exploration on anion ordering, optical properties and electronic structure in K₃WO₃F₃ elpasolite. *J. Solid State Chem.* **187**, 159–164 (2012)
36. A.M. El Nahrawy, A. Elzawy, A.B.A. Hammad, A.M. Mansour, Influence of NiO on structural, optical, and magnetic properties of Al₂O₃-P₂O₅-Na₂O magnetic porous nanocomposites nucleated by SiO₂. *Solid State Sci.* **108**, 106454 (2020)
37. V.R. Akshay, B. Arun, G. Mandal, M. Vasundhara, Visible range optical absorption, Urbach energy estimation and paramagnetic response in Cr-doped TiO₂ nanocrystals derived by a sol–gel method. *Phys. Chem. Chem. Phys.* **21**, 12991–13004 (2019)
38. S.M. Yakout, Influence of Na and Na/Fe doping on the dielectric constant, ferromagnetic and sunlight photocatalytic properties of BaTiO₃ perovskite. *J. Solid State Chem.* **290**, 121517–121527 (2020)
39. S. Kanchana, M.J. Chithra, S. Ernest, K. Pushpanathan, Violet emission from Fe doped ZnO nanoparticles synthesized by precipitation method. *J. Lumin.* **176**, 6–14 (2016)
40. D.Y. Inamdar, A.K. Pathak, I. Dubenko, N. Ali, S. Mahamuni, Room temperature ferromagnetism and photoluminescence of Fe doped ZnO nanocrystals. *J. Phys. Chem. C.* **115**, 23671–23676 (2011)
41. N. Kati, Investigation of optical and morphological properties of Co doped ZnO nanomaterial. *Turk. J. Sci. Technol.* **14**, 41–48 (2019)
42. Y.G. Denisenko, M.S. Molokeev, A.S. Oreshonkov, A.S. Krylov, A.S. Aleksandrovsky, N.O. Azarapin, O.V. Andreev, I.A. Razumkova, V.V. Atuchin, Crystal structure, vibrational, spectroscopic and thermochemical properties of double sulfate crystalline hydrate [CsEu(H₂O)₃(SO₄)₂].H₂O and its thermal dehydration product CsEu(SO₄)₂. *Crystals* **11**, 1027–1051 (2021)
43. N.N. Golovnev, M.S. Molokeev, S.N. Vershchagin, V.V. Atuchin, Calcium and strontium thiobarbiturates with discrete and polymeric structures. *J. Coord. Chem.* **66**, 4119–4130 (2013)

44. N.N. Golovnev, M.S. Molokeev, M.K. Lesnikov, V.V. Atuchin, First outer-sphere 1,3-diethyl-2-thiobarbituric compounds $[M(H_2O)(6)](1,3\text{-diethyl-2-thiobarbiturate})_2$ center dot $2H_2O$ ($M = Co^{2+}, Ni^{2+}$): crystal structure, spectroscopic and thermal properties. *Chem. Phys. Lett.* **653**, 54–59 (2016)
45. A. Kumar, M.K. Warshi, V. Mishra, S.K. Saxena, R. Kumar, P.R. Sagdeo, Strain control of Urbach energy in Cr-doped $PrFeO_3$. *Appl. Phys. A* **123**, 576–583 (2017)
46. L.P. Chanu, S. Phanjobam, Study on the structural and electrical properties of $YMnO_3$ co-substituted with transition metal ions at Mn-site and their conduction mechanism. *J Mater Sci: Mater Electron.* **33**, 6107–6120 (2022)
47. K.C.B. Naidu, V.N. Reddy, T.S. Sarmash, D. Kothandan, T. Subbarao, N.S. Kumar, Structural, morphological, electrical, impedance and ferroelectric properties of $BaO-ZnO-TiO_2$ ternary system. *J. Aust. Ceram. Soc.* **55**, 201–218 (2019)
48. A. Manohar, C. Krishnamoorthi, K.C.B. Naidu, B. Narasaiah, Dielectric, magnetic hyperthermia and photocatalytic properties of $Mg_{0.7}Zn_{0.3}Fe_2O_4$ nanocrystals. *IEEE Trans. Magn.* **56**, 5200207–5200234 (2020)
49. M. Salah, S. Azizi, A. Boukhaem, C. Khaldi, M. Amlouk, J. Lamoumi, Rietveld refinement of X-ray diffraction, impedance spectroscopy and dielectric relaxation of Li-doped ZnO-sprayed thin films. *Appl. Phys. A* **615**, 125–145 (2019)
50. S.E.L. Kossi, C. Rayssi, A.H. Dhahri, J. Dhahri, K. Khirouni, High dielectric constant and relaxor behavior in $La_{0.7}Sr_{0.25}Na_{0.05}Mn_{0.8}Ti_{0.2}O_3$ manganite. *J. Alloys Compd.* **767**, 456–463 (2018)
51. A.M.El. Nahrawy, B.A. Hemdan, A.B.A. Hammad, Morphological, impedance and terahertz properties of zinc titanate/ Fe^{3+} nanocrystalline for suppression of *Pseudomonas aeruginosa* biofilm. **26**, 100715–100727 (2021)
52. S.A. Ansari, A. Nisar, B. Fatma, W. Khan, A.H. Naqvi, Investigation on structural, optical and dielectric properties of Co doped ZnO nanoparticles synthesized by gel combustion route. *Mater. Sci. Eng. B* **177**, 428–435 (2012)
53. A.M.El. Nahrawy, A.B.A. Hammad, A.M. Bakr, A.R. Wassel, Adjustment of morphological and dielectric properties of $ZnTiO_3$ nanocrystalline using Al_2O_3 nanoparticles. *Appl. Phys. A* **125**, 54–51 (2019).
54. O. Gürbüz, M. Okutan, Structural, electrical, and dielectric properties of Cr doped ZnO thin films: role of Cr concentration. *Appl. Surf. Sci.* **387**, 1211–1218 (2016)
55. C. Belkhaoui, N. Mzabi, H. Smaoui, P. Daniel, Enhancing the structural, optical and electrical properties of ZnO nanopowders through (Al + Mn) doping. *Results Phys.* **12**, 1686–1696 (2019)
56. B. Askri, I. Riahi, R. Mimouni, M. Amlouk, Photoluminescence and dielectric properties of (Al/Cu) and (In/Cu) co-doped ZnO sprayed thin films under the oxygen deficiency framework. *Superlattices Microstruct.* **150**, 106731–106752 (2021)
57. H.M. Ahsan, K. Lal, M. Saleem, G.M. Mustafa, M.A. Khan, A.S. Haidyrah, S. Atiq, Tuning the dielectric behavior and energy storage properties of Mn/Co co-doped ZnO. *Mater. Sci. Semicond. Process.* **134**, 105977–105985 (2021)
58. M. Ashokkumar, S. Muthukumaran, Effect of Cr-doping on dielectric, electric and magnetic properties of $Zn_{0.96}Cu_{0.04}O$ nanopowders. *Powder Technol.* **268**, 80–85 (2014).
59. S. Das, S. Das, S. Sutradhar, Effect of Gd^{3+} and Al^{3+} on optical and dielectric properties of ZnO nanoparticle prepared by two-step hydrothermal method. *Ceram. Int.* **43**, 6932–6941 (2017)
60. J. Jadhav, S. Biswas, Structural and electrical properties of ZnO: Ag core-shell nanoparticles synthesized by a polymer precursor method. *Ceram. Int.* **42**, 16598–16610 (2016)
61. A.M.El. Nahrawy, A.M. Bakr, B.A. Hemdan, A.B.A. Hammad, Identification of Fe^{3+} co-doped zinc titanate mesostructures using dielectric and antimicrobial activities. *Int. J. Environ. Sci. Technol.* **17**, 4481–4494 (2020).
62. N. Bhakta, P.K. Chakrabarti, XRD analysis, Raman, AC conductivity and dielectric properties of Co and Mn co-doped SnO_2 nanoparticles. *Appl. Phys. A* **73**, 125–135 (2019)
63. O. Polat, M. Coskun, F.M. Coskun, J. Zlamal, B.Z. Kurt, Z. Durmus, M. Caglar, A. Turut, Co doped $YbFeO_3$: exploring the electrical properties via tuning the doping level. *Ionics* **25**, 4013–4029 (2019)
64. S. Khera, P. Chand, Influence of different solvents on the structural, optical, impedance and dielectric properties of ZnO nanoflakes. *Chin. J. Phys.* **57**, 28–46 (2019)
65. Y. Zulfikar, J. Yuan, W. Yang, Z. Wang, J. Ye, Lu, Structural, dielectric and ferromagnetic behavior of (Zn, Co) co-doped SnO_2 nanoparticles. *Ceram. Int.* **42**, 17128–17136 (2016)
66. R.D. Shannon, Dielectric polarizabilities of ions in oxides and fluorides. *Appl. Phys.* **73**, 348–366 (1993)
67. P. Norouzzadeh, Kh. Mabhouti, M.M. Golzan, R. Naderali, Effect of Mn-substitution on impedance spectroscopy and magnetic properties of Al-doped ZnO nanoparticles. *Optik* **31**, 1–32 (2020)
68. F. Mizouri, N. Abdelmoula, D. Mezzane, H. Khemakhem, Impedance spectroscopy and conduction mechanism of multiferroic $Bi_{0.8}(Ba_{0.9}Ca_{0.1})_{0.8}Fe_{0.8}(Ti_{0.9}Sn_{0.1})_{0.8}O_3$. *J. Alloys Compd.* **763**, 570–580 (2018)

Publisher's Note Springer Nature remains neutral with regard to jurisdictional claims in published maps and institutional affiliations.